www.sciencemag.org/content/349/6246/408/suppl/DC1

Supplementary Materials for

Coherent coupling of a single spin to microwave cavity photons

J. J. Viennot,* M. C. Dartiailh, A. Cottet, T. Kontos*

*Corresponding author. E-mail: viennot@lpa.ens.fr (J.J.V.); kontos@lpa.ens.fr (T.K.)

Published 24 July 2015, *Science* **349**, 408 (2015)
DOI: 10.1126/science.aaa3786

This PDF file includes:

Materials and Methods

Double quantum dot susceptibility at zero magnetic field

Similarly to previous hybrid cavity– quantum dot experiments, two different physical quantities can be measured on the device. We can perform a DC transport measurement, acquiring the current flowing through the double quantum dot as a function of gate voltages. This allows us to obtain a conventional transport spectroscopy as shown in figure S1. We can simultaneously measure the phase and amplitude of the microwave field transmitted through the cavity, which is sensitive to the susceptibility of the double quantum dot transitions. Figure S1 shows such measurements in a gate region where the carbon nanotube device behaves as a double quantum dot. These color-scale plots outline the stability diagram of the device in this region, at zero external magnetic field. We label the charge occupation numbers of the dots by n and m. At the degeneracy between the dot's left/right charge occupation states (n,m+1) and (n+1,m), we observe sign changes in the phase signal along two parallel lines indicating transitions in the double quantum dot that are resonant with the microwave cavity.

Measurement techniques

The microwave measurement techniques are essentially similar to those used in ref *(26)*. We measure the amplitude and the phase of the transmitted microwave signal as a function of the various parameters of the system (frequency of drive, magnetic field or DC gate voltages) either using a heterodyne detection scheme or a Vector Network Analyzer (VNA).

For every change in magnetic field, we first search and measure the bare cavity frequency f_c by strongly detuning all the DQD transitions from the cavity (typically by going to $\varepsilon > 1$mV). We measure the cavity linewidth and the frequency dependence of the phase at maximum transmission (phase slope). The latter gives the phase sensitivity to a resonant frequency change. We acquire precisely the bare (i.e. the reference) phase and amplitude, then we tune the double dot, going back to ε values given in the data and subsequently measure phase and amplitude shifts from their bare value, namely $\Delta\varphi$ and $\Delta A/A$. This allows us to compensate for the weak dependence of f_c on magnetic field, and for the jumps associated to magnetic flux vortices penetrating the superconducting film (see ref 8).

Fabrication method

A 150nm thick Nb film is first evaporated on an RF Si substrate at rate of 1nm/s and a pressure of 10^{-9} mbar. The cavity is made subsequently using photolithography combined with reactive ion etching (SF_6 process). Carbon nanotubes are grown with Chemical Vapor Deposition technique (CVD) at about 900°C using a methane process on a separate quartz substrate and stamped onto the device chip in the desired location inside the gap of the cavity *(31)*. The nanotubes are then localized and contacted in two e-beam lithography steps with top gates and PdNi source and drain contacts, which carry DC signals, as shown in figure 1A and 1B. The top gates are a multilayer of 6nm of Al_2O_3 covered with 50 nm of Al and 20nm of Pd. The Al_2O_3 is obtained in 3 steps by

evaporating 2nm of Al and oxidizing this layer by letting 1mbar of O_2 for 10 min. The PdNi source drain electrodes are 30nm thick, 150nm wide $Ni_{75}Pd_{25}$ layers capped with a 5nm Pd layer.

Determination of decoherence and spin-photon coupling strength

In order to derive the transmission coefficient of the cavity, we first consider one transition between energy levels i and j in the double dot, coupled to the cavity mode. From the traditional Jaynes-Cummings Hamiltonian, we write the conventional equations of motion :

$$\frac{d}{dt}a = -(\kappa/2 + i\Delta)a + \sqrt{\kappa_1}a_{in,1} + \sqrt{\kappa_2}a_{in,2} - ig_{ij}\sigma_-$$

$$\frac{d}{dt}\sigma_- = -(\Gamma_{ij}/2 + i\Delta_{ij})\sigma_- + ig_{ij}a\sigma_z$$

$$\frac{d}{dt}\sigma_z = -\gamma_{ij}(\sigma_z + 1) - 2ig_{ij}(a\sigma_+ - a^+\sigma_-)$$

where a is the annihilation operator of the cavity field, $a_{in(out),1(2)}$ are annihilation operators for fields propagating inwards (outwards) the cavity at port 1 (2), $\kappa = \kappa_{\text{int}} + \kappa_1 + \kappa_2$ is the total cavity decay given by the sum of internal loss and coupling to the two ports of the resonator. Above, g_{ij} is the coupling constant of the transition to the resonator, Γ_{ij} its total decoherence rate (relaxation + dephasing), γ_{ij} its relaxation rate, and Δ_{ij} its detuning to the drive frequency. We introduce the Pauli operator σ_z associated to the transition, and the lowering and raising operators σ_-, σ_+.

We now write the input-output relation in which we add a small correction arising from the direct parasitic (and weak) transmission channel in our sample holder :

$$a_{\text{out},2} \approx -i\sqrt{T}e^{i\zeta}\ a_{\text{in},1} + \sqrt{1-T}\ \mathrm{e}^{i(\zeta-\theta)}\ a_{\text{in},2} + \sqrt{\kappa_2}\ a$$

Above, T and ζ account for the amplitude and phase of the direct parasitic (and weak) transmission channel in our sample holder and κ_2 is the coupling rate of the cavity to port 2. The $\approx$ sign indicates that such an equation is only valid at lowest order in T and does not ensure unitarity of the scattering matrix for arbitrary values of T.

In the semi-classical limit, we make use of the usual decoupling $\langle a\sigma_z\rangle \approx \langle a\rangle\langle\sigma_z\rangle, \langle a\sigma_+\rangle \approx \langle a\rangle\langle\sigma_+\rangle, \langle a^+\sigma_-\rangle \approx \langle a\rangle^*\langle\sigma_-\rangle$ and compute the transmission coefficient $S_{21} = \langle a_{out,2}\rangle / \langle a_{in,1}\rangle$:

$$S_{21} = \frac{\alpha}{2\pi(f_{cav} - f) - i\kappa/2 - \dfrac{g_{ij}^{\ 2}}{-i\Gamma_{ij}/2 + \Delta_{ij}}} - i\sqrt{T}e^{i\zeta}$$

with $\Delta_{ij} = 2\pi(f_{ij} - f)$, f_{ij} being the double quantum dot transition frequency, f_{cav} being the resonance frequency of the cavity and f being the frequency of the cavity drive. The parameter $\alpha = \sqrt{\kappa_1\kappa_2}$ accounts for the coupling capacitance of the resonator and *T* and ζ control the Fano line shape of our resonance, which is slightly visible in figure 3B.

The above formula is the one used to fit the transmission of the cavity as shown in figure 3B in the main text. First, the cavity parameters (α, κ, f_{cav}, *T*, ζ) are extracted when the double dot is strongly detuned (all the χ_{ij}=0). After determining the resonance point $\Delta_{ij} = 0$, we fit the data with two free parameters, g_{ij} and Γ_{ij}. This allows us to extract both the cooperativity and the dephasing rate of the transition *ij*. In addition, whereas the Fano line shape is important to obtain a quantitative fit of the resonances both tuned and detuned, letting *T* to zero does not give markedly different cooperativies and decoherence rates (in this case one has to correct for the background of the data). The amplitude *A* is defined as $|S_{21}|$ and the phase φ as $\arg(S_{21})$.

It is important to stress that the cooperativity controls the maximum of the resonance whereas the decoherence rate controls the width. Hence, the cooperativity can also be directly extracted from the ratio of the transmission at resonance in the tuned and detuned condition. Indeed, one can show that the above formula leads to:

$$C_{ij} = \frac{4g_{ij}^{\ 2}}{\kappa\Gamma_{ij}} \approx \frac{A_{OFF}}{A_{ON}} - 1$$

Applying this formula yields C=2.3, in very good agreement with the full fitting procedure for the data in figure 3B. The approximate equality stems from the slight Fano line shape and becomes exact if *T=0*.

Theory of our experimental findings

We further support our experimental findings by a microscopic modeling of our nanotube based spin/photon coupling scheme. The starting point is the full microscopic Hamiltonian of the carbon nanotube based double quantum dot with non-collinear ferromagnetic contacts, projected onto the (1,0)-(0,1) charge states, and coupled to a single mode of the cavity. Since the double quantum dot which we study is made out of a single wall carbon nanotube, we must include the K/K' valley degree of freedom in the description (not represented in figure 2D for the sake of simplicity). The full Hamiltonian reads :

$$
\begin{aligned}
H_d = & \\
& -\frac{(1+\hat{\tau}_Z)}{2}\frac{(\vec{\delta}_{L,K}(1+\hat{\gamma}_Z)+\vec{\delta}_{L,K'}(1-\hat{\gamma}_Z)+\alpha_{spin}^{L}\mu_B\vec{B}_{ext})}{2}.\vec{\hat{\sigma}} \\
& -\frac{(1-\hat{\tau}_Z)}{2}\frac{(\vec{\delta}_{R,K}(1+\hat{\gamma}_Z)+\vec{\delta}_{R,K'}(1-\hat{\gamma}_Z)+\alpha_{spin}^{R}\mu_B\vec{B}_{ext})}{2}.\vec{\hat{\sigma}} \\
& +(t\hat{\tau}_x+\varepsilon\hat{\tau}_Z)\hat{\gamma}_0\hat{\sigma}_0-\frac{1}{2}\alpha_{orb}\mu_B B_{ext}\hat{\gamma}_z\hat{\tau}_0\hat{\sigma}_0+\Delta_{KK'}\hat{\gamma}_x\hat{\tau}_0\hat{\sigma}_0 \\
& +g_d(a+a^+)\hat{\tau}_z\hat{\gamma}_0\hat{\sigma}_0+\hbar\omega_{cav}a^+a
\end{aligned}
$$

with

$$\vec{\delta}_{L(R),K/K'}=\delta_{L(R),K/K'}(\cos\theta_{L(R)}\vec{u}_z+\sin\theta_{L(R)}\vec{u}_x)$$

Here, $\vec{\hat{\sigma}}$ is the spin operator, $\hat{\gamma}_i, i\in\{x,y,z\}$ are the Pauli matrices acting in the valley space and $\hat{\tau}_i, i\in\{x,y,z\}$ are the Pauli matrices acting in the L/R space of the double quantum dot. The unit vector in the direction $x(z)$ is denoted by $\vec{u}_{x(z)}$. The vectors $\vec{\delta}_{L,K}, \vec{\delta}_{L,K'}, \vec{\delta}_{R,K}, \vec{\delta}_{R,K'}$ are the valley/dot dependent effective magnetic fields induced by the ferromagnetic contacts. We define the detuning ε and the hopping constant t between the left(L) and the right(R) dots. We use effective spin and orbital Landé factors $\alpha_{spin}^{L(R)}$ and $\alpha_{orb}^{L(R)}$. We assume that there can be a small disorder induced valley mixing which we include in the usual way with a phenomenological parameter $\Delta_{KK'}$. Finally, the interaction between the cavity photons and the double quantum dot is characterized by the coupling strength g_d. The cavity frequency is ω_{cav}.

Since the measurements of Figures 2 and 3 are realized with a slowly varying magnetic field, they do not show the hysteretic behavior of Figure 4. Instead, the magnetizations are relaxed for each measurement point in equilibrium positions described by angles θ_L and θ_R which vary with B_{ext}. For simplicity we use:

$$\theta_{L(R)}=\theta_{L(R)}^0\exp(-{}^{B_{ext}}\!/_{B_0}) \text{ for } B_{ext}>0$$
$$\theta_{L(R)}=\pi+\theta_{L(R)}^0\exp({}^{B_{ext}}\!/_{B_0}) \text{ for } B_{ext}<0$$

These equations take into account that the magnetizations and the external magnetic field tend to the same direction for high values of B_{ext}. They also take into account that for a vanishing B_{ext}, the orientations of the magnetizations stick to the easy axis of the electrodes, but with a π-flip from $B_{ext}>0$ to $B_{ext}<0$, in order to minimize the angle with the magnetic field. This last feature is essential to reproduce the cusps occurring in the resonances of Fig. 2A and 2B for $B_{ext}=0$.

The above Hamiltonian is a generalization of the Hamiltonian (1) of *(15)* in which the valley degree of freedom was omitted. The inhomogeneity in the direction of the effective fields ($\theta_L\neq\theta_R$) induces a mixing of the spin states and the L/R orbital states.

This is the main ingredient for our artificial spin orbit interaction. Since the photons induce electron hopping between the left and the right dot, they can also induce spin flips.

We determine from the Hamiltonian the transition energies $E_{ij}=h\,f_{ij}$, and the couplings g_{ij}. We also include in the model decoherence rates Γ_{ij}, which include relaxation and dephasing. For simplicity we use a small transition independent relaxation rate Γ_1. In our model, decoherence is dominated by charge noise treated semiclassically up to second order in order to describe properly sweet spots. Using the above equations and the transmission formula given in the previous section, we obtain the full colorscale plots of the amplitude and phase of the microwave signal as a function of the gate detuning ε and the external magnetic field B_{ext} (see Figure S5). This allows us to account very well for the measurements presented in Figures 2A and 2B as well as the spectroscopic lines of Figure 3. We use the following parameters : $\omega_{cav}=6735\,MHz$, $t=2380\,MHz$, $\delta_{L,K}=3135\,MHz$, $\delta_{L,K'}=3095\,MHz$, $\delta_{R,K}=3145\,MHz$, $\delta_{R,K'}=3100\,MHz$, $\alpha_{spin}^{K}\mu_B=2700\,MHz/T$, $\alpha_{spin}^{K'}\mu_B=1300\,MHz/T$, $\alpha_{orb}\mu_B=300\,MHz/T$, $\Delta_{KK'}=28\,MHz$, $g_d=45MHz$, $\Gamma_1=1MHz$, $B_0=1{,}5\,T$, $\theta_L^0=-0.17\,rad$, and $\theta_R^0=\theta_L^0+\frac{\pi}{4}$. We show in Figure S4 the DQD eigenenergies obtained from Hamiltonian H_d and the corresponding transitions energies E_{ij}, versus B_{ext}. The number of eigenstates is twice larger than expected from figure 2D, due to the inclusion of the K/K' degree of freedom. The two lowest eigenstates 0 and 1 of H_d are only slightly split due to the slight asymmetry between the K and K' valleys. With the above parameters and the B_{ext} values of the experiment, this splitting is smaller than temperature. Therefore, we assume that these two states are equally populated. From Figure S4B, the transitions 04, 15 and 25 become resonant with the cavity. They reproduce well the transitions Spin, Spin' and the third faint transition of the main text, respectively.

With the above model, the doublets in figure S5C and D arise from the slight asymmetry between the K and K' valleys. Note that the coupling between the two valleys remains very small here. With our parameters, the two strong resonances from the doublet (04 and 15) are dominated by spin-flip and (to a weaker proportion) by L/R flips. These two transitions are mainly valley conserving. Their contrast is rather well reproduced by our simulation, which confirms that decoherence of our spin states is indeed to a great extent caused by charge noise, due to the spin/charge hybridization. In particular, we can reproduce the existence of a minimum of decoherence and a maximum in the spin-photon cooperativity near $\varepsilon=0$. This behavior is due to the existence of a sweet spot with respect to charge noise, indicated by the green dotted line in Fig.S5C. In constrast, the third faint resonance (25) has a more important K/K' flip component. The contrast of this resonance is stronger in the calculation than in the data, which may be corrected by introducing a specific intrinsic K/K' relaxation rate. Indeed, the K/K' degree of freedom is expected to be intrinsically less coherent than the spin degree of freedom because it can be directly affected by spin-conserving decoherence sources such as phonons.

Note that in our experiment, we could not determine the parity of the DQD states. We have chosen to use a one electron model because it reproduces well the data. It is

nevertheless important to point out that in principle, the parity of the electron states should affect only quantitatively the behavior of our device. Indeed, the concept of an artificial spin-orbit coupling induced by non-collinear ferromagnetic contacts remains valid for even occupation states. The robustness of this principle is a significant advantage of our scheme.

Hysteresis measurements

We use a standard definition of the magneto-conductance $\frac{I_{DC}^{\ incr} - I_{DC}^{\ decr}}{I_{DC}^{\ incr} + I_{DC}^{\ decr}}$. Because the phase signal can have both sign, we normalize the phase variations slightly differently to avoid large divergences when transitions are resonant with the cavity. We define the magneto-phase as $\frac{\Delta\varphi^{incr} - \Delta\varphi^{decr}}{\left|\Delta\varphi^{incr}\right| + \left|\Delta\varphi^{decr}\right|}$.

It is important to check that the hysteresis we observe in the phase of the cavity is due to the susceptibility of the coupled spin transitions and does not arise from spurious hysteretic behavior of the bare cavity mode. Figure S6 shows the bare superconducting cavity characteristics for increasing and decreasing magnetic field, and their hysteresis in percent. The presented data are extracted during the same magnetic field cycle as in figure 4 of the main text. They are acquired for far detuned double quantum dot transitions, as explained above. In the main text, our purpose is to detect the phase variation caused by the DQD , which is given by $\Delta\varphi \sim$ (phase slope)$\times$Re(χ_{ij}) at first order in the DQD/cavity coupling. In figure 4D of the main text, the observed hysteresis of the phase shift reaches more than 50% at small fields and up to 100% at DQD/cavity resonances. In contrast, the bare cavity parameters all show a small hysteresis, from less than 0.1% for the resonant frequency to few percent for cavity linewidth and phase slope at resonance, with qualitatively different variations from figure 4D. Therefore the data of the main text are not due to a simple hysteresis from the cavity.

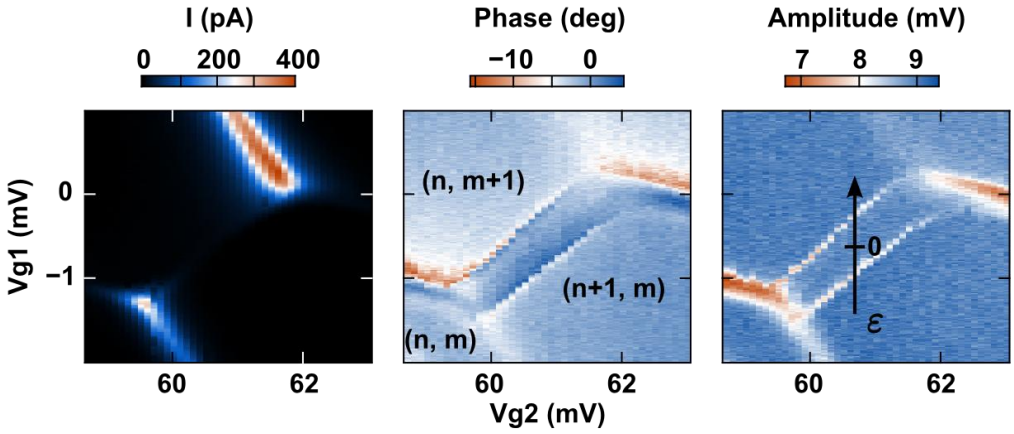

Fig. S1.

Stability Diagram. Double quantum dot transport spectroscopy showing the region on the stability diagram studied in the paper (V_{gt} = -1mV, B_{ext} = 0mT). Left panel shows a color-scale plot of the DC current ($V_{SD} \approx 20\mu V$). Middle and right panels show phase and amplitude of the transmission coefficient S_{21}, see SM text. Stable charges states are labeled by (n,m) with n and m occupation numbers in each dot.

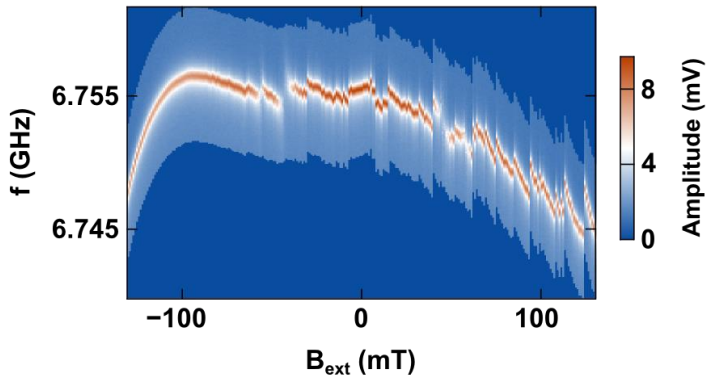

Fig. S2

Cavity transmission in absolute frequency. Measured transmission spectrum of the cavity as a function of B_{ext} without post-treament.

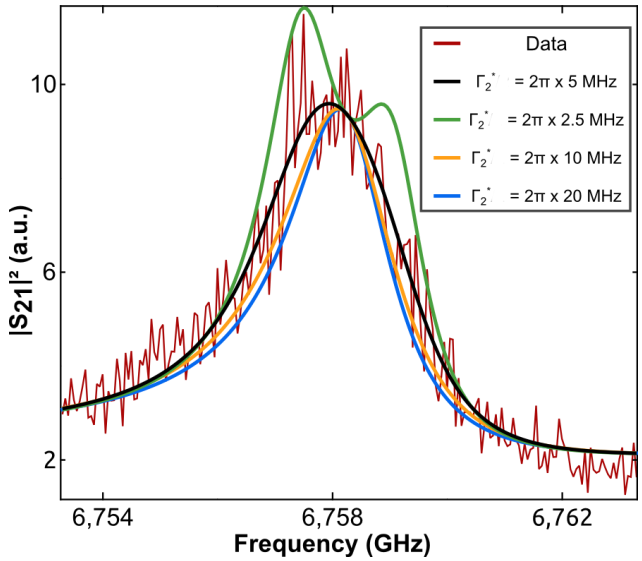

Fig. S3

Extracting the decoherence rate. Transmission of the cavity at -67 mT, when the spin transition is brought in resonance with the cavity (as described in the main text). The black curve is the best fit and the other curves correspond to different spin decoherence rates.

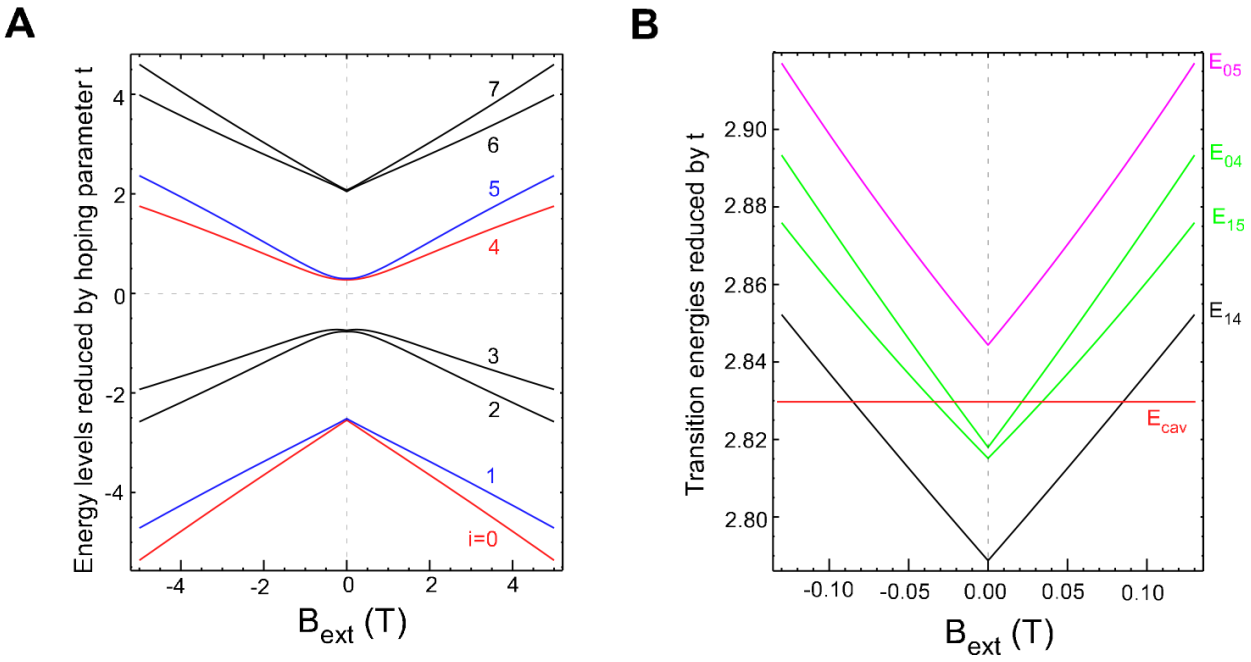

Fig. S4

Spectrum obtained from the theoretical model. (A) and (B) Calculated DQD energy spectrum and transition energies E_{ij} versus B_{ext}, for ε=0 and the parameters given in the section "Theory of our experimental findings". The energy levels are labelled with an index i. For the B_{ext} values used experimentally, the transitions energies E_{04}, E_{15}, and E_{04} can become resonant with the cavity. We have only represented the transitions which are close to the cavity for the sake of clarity.

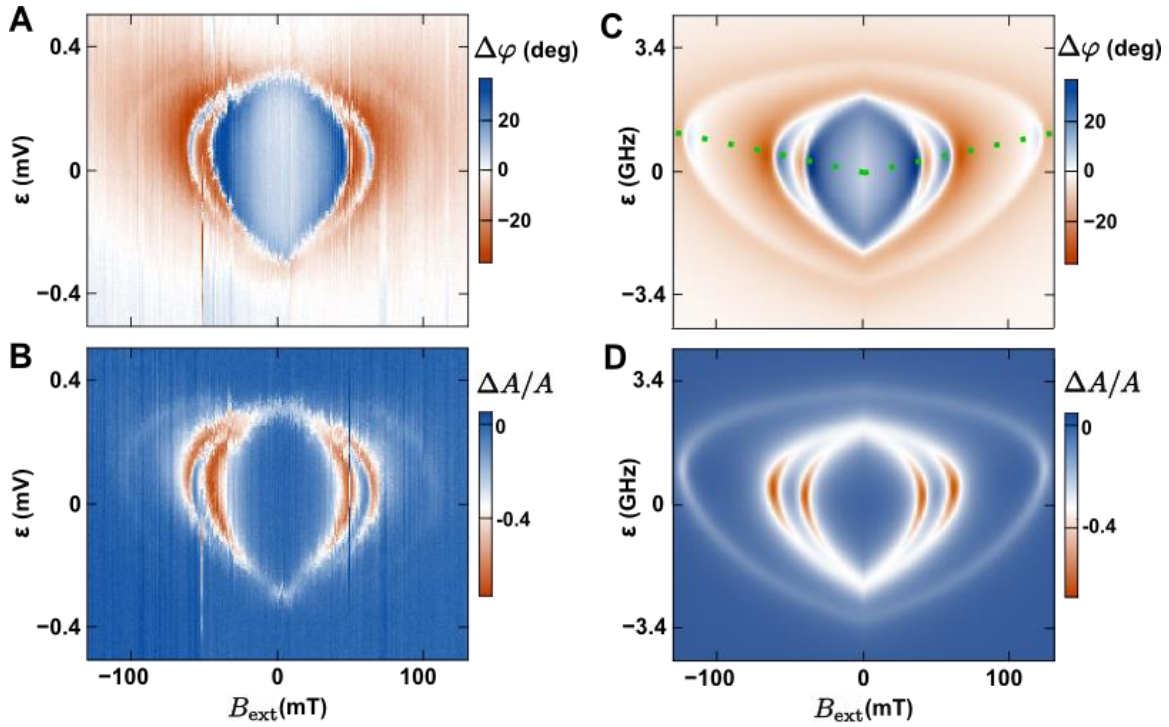

Fig. S5

Electric and magnetic dependence of the transitions: experiment and theoretical model. (A) and (B) phase and amplitude measured as in the main text. (C) and (D) modelling of the phase and amplitude using the microscopic Hamiltonian described in the SM. The green dotted line in panel C corresponds to a sweet spot with respect to charge noise.

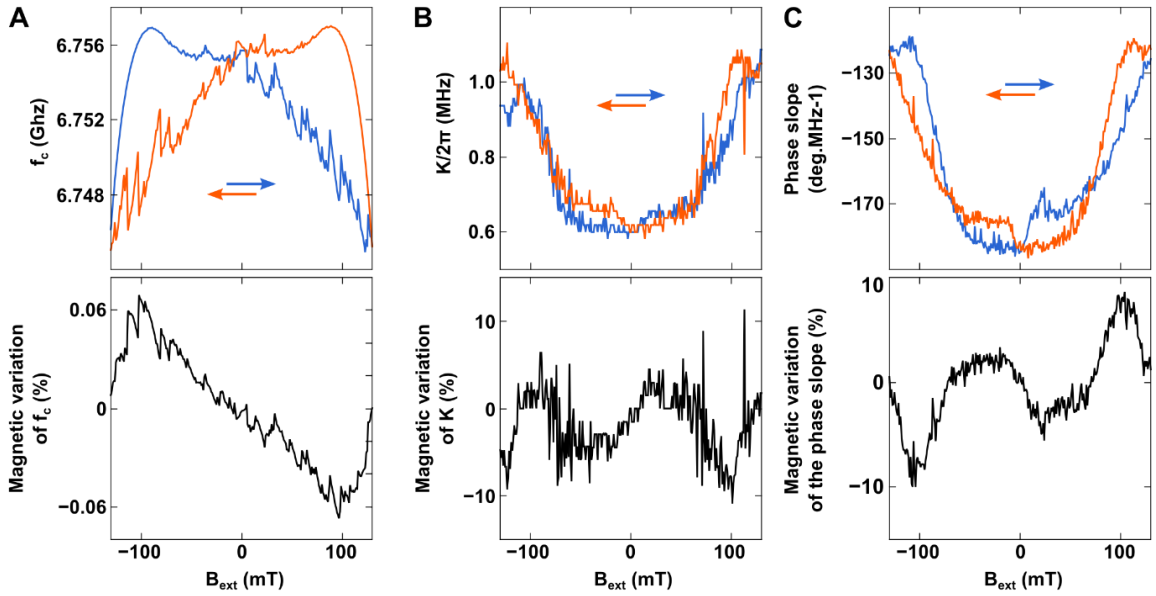

Fig. S6

Hysteresis of the cavity properties. Bare superconducting resonator characteristics (double quantum dot transitions far detuned) as a function of magnetic field and magnetic field sweep direction. (A) Resonant frequency. (B) Cavity linewidth. (C) Phase slope at resonance.